Eur. Phys. J. B **60**, 447–462 (2007)
DOI: 10.1140/epjb/e2008-00005-5

**THE EUROPEAN
PHYSICAL JOURNAL B**

Fluid-fluid interaction during miscible and immiscible displacement under ultrasonic waves

T. Hamida[a] and T. Babadagli[b]

University of Alberta, Department of Civil and Environmental Engineering, School of Mining and Petroleum, 3-112 Markin CNRL-NREF, Edmonton, AB, Canada T6G 2W2

Received 27 February 2007 / Received in final form 9 September 2007

Abstract. This paper aims at identifying and analyzing the influence of high-frequency, high-intensity ultrasonic radiation at the interface between immiscible (different types of oils and aqueous solutions) and miscible (different types of oil and solvent) fluids. An extensive set of Hele-Shaw type experiments were performed for several viscosity ratios, and interfacial tension. Fractal analysis techniques were applied to quantify the degree of fingering and branching. This provided a rough assessment of the degree of perturbation generated at the interface when the capillary forces along with the viscous forces are effective. Miscible Hele-Shaw experiments were also presented to isolate the effect of viscous forces. We found that ultrasound acts to stabilize the interfacial front, and that such effect is most pronounced at low viscosity ratios.

PACS. 47.15.gp Hele-Shaw flows – 47.27.eb Statistical theories and models – 47.61.Jd Multiphase flows – 43.35.-c Ultrasonics, quantum acoustics, and physical effects of sound

1 Introduction

Laboratory and field scale applications showed that high and low frequency acoustic waves may cause an increase in oil recovery [1–10]. The authors of the present study have previously studied the interface between the displacing and displaced phases and observed considerable changes at the interface and oil recovery when ultrasonic energy is introduced [11–13]. The exact mechanism behind ultrasonic stimulation, however, is still poorly understood. This is mainly due to the complexity of the process and the superposition of several competing effects. To scrutinize the effect of ultrasound on the displacement process, Hele-Shaw type experiments, which focus on ultrasonically induced perturbations at the liquid-liquid interface are presented in the present study. Such experiments primarily focus on viscous forces, and therefore suppress the effects due to capillary forces.

When a viscous fluid is displaced by a less viscous fluid, one observes finger-like displacement patterns known as "viscous fingers". Since Saffman and Taylor's pioneering work [14], viscous fingering has been subject of extensive research in various disciplines such as flow through porous media, combustion in two dimensions, and electrochemical deposition. The Hele-Shaw cell, made up of two parallel plates separated by a thin spacer, is used to explore viscous fingering in 2 dimensions. The flow is governed by the Hele-Shaw equation for Newtonian fluid films:

$$u_i = \frac{-b}{12\mu_i} \nabla P_i \tag{1}$$

where the subscript refers to the fluid phase, u_i is the depth averaged velocity within the cell of thickness b, μ_i is the dynamic fluid viscosity and P_i is the fluid pressure. Note that this equation reduces to a Laplacian formulation in the case of incompressible fluids, i.e. when $\nabla \mathbf{u}_i = 0$. In the presence of an interface, as is the case with immiscible fluids, the pressure differential at the interface is related to the interfacial tension and the curvature of the interface as defined by the Young-Laplace equation:

$$P_1 - P_2 = \sigma \left(\frac{1}{r_1} - \frac{2\cos\theta}{b} \right) \tag{2}$$

where r_1 is the horizontal curvature of the interface. σ denotes the interfacial tension and θ is the contact angle between phase 1 and phase 2. The growing fingers continuously split into sub-branches due to the interfacial instability at the liquid-liquid interface, thereby generating a fractal structure whose smallest element is determined by a balance between viscous and interfacial forces. The morphology of viscous fingers has been studied extensively by Mclean and Saffman [15], Park and Homsy [16], and

---

[a] Now with Alberta Research Council, Edmonton, AB, Canada

[b] e-mail: `tayfun@ualberta.ca`

Maxworthy [17], and can be described by the modified capillary number [18,19]

$$Ca' = \frac{U\mu}{\sigma b^2} \tag{3}$$

where U is the volumetric velocity of the fluid at the interface, μ the dynamic viscosity of the displaced fluid, σ the interfacial tension, and b the spacing between the plates. In order to generate a complex fingering pattern, one must minimize the characteristic length scale λ_c [20,21], defined as

$$\lambda_c = \pi b \sqrt{\frac{\sigma}{\mu U}}. \tag{4}$$

This instability length is sometimes called the capillary length and represents the most unstable wavelength from linear instability analysis between two immiscible fluids with high viscosity ratio [20]. The capillary length is small when b and σ are small, and μ and U are large [22]. The different mechanisms of finger splitting, shielding and spreading are thoroughly discussed by Homsy [23].

One striking feature of viscous finger growth within a planar geometry is that the propagation of a Laplacian flow field has a close similarity to the growth of aggregates generated by Diffusion Limited Aggregation (DLA) [24–26]. Whether there is a mathematical correspondence between these distinctively different processes is still under debate.

Since most of the governing mechanisms behind ultrasonic stimulation are dominated by interfacial forces, it was hoped to gain valuable insights into interfacial behavior from Hele-Shaw experiments. In fact, Hele-Shaw experiments very accurately illustrate how perturbations influence the liquid-liquid interface, without the additional complexity arising from porous (channeled) structures, such as rocks. Since ultrasound introduces a perturbation in the form of pressure fluctuations, one would expect to observe a more complex pattern than with viscous fingering in the absence of ultrasound. This is partially due to the fact that ultrasound adds additional points of instability at the interface. However, this effect needs to be tested. Any change on the fractal morphology of the interface would indicate that the ultrasound introduces a perturbation onto the interface, which either enhances or reduces the complexity of the fingering pattern. High complexity of the interface is an indication of more severe frontal instability, and is directly related to the effective capillary number of the system. This change in complexity can be quantified by use of fractal dimension. May and Maher [27] measured the fractal dimension for a wide range of capillary numbers (N_{Ca}'), and found that the fractal dimension took on the value of approximately 1.71 for N_{Ca}' between a critical value and 35, and 1.79 at intermediate values, after which it plateaus at 1.79.

To gain more insight into the capillary interaction between oil and aqueous phase, we designed a series of immiscible Hele-Shaw experiments at constant pressure and injection rate. A similar approach as employed by Fernandez and Homsy [28] was adopted. They studied the change in fingering patterns in a Hele-Shaw cell during a chemical reaction, and used fractal methods and dimensionless groups, to quantify changes in interfacial tension during the exothermal heating of the front. Additionally, we performed a series of miscible, high viscosity-ratio Hele-Shaw experiments, where interfacial phenomena are entirely absent and the process is entirely dominated by viscous forces, mechanical dispersion and molecular diffusion.

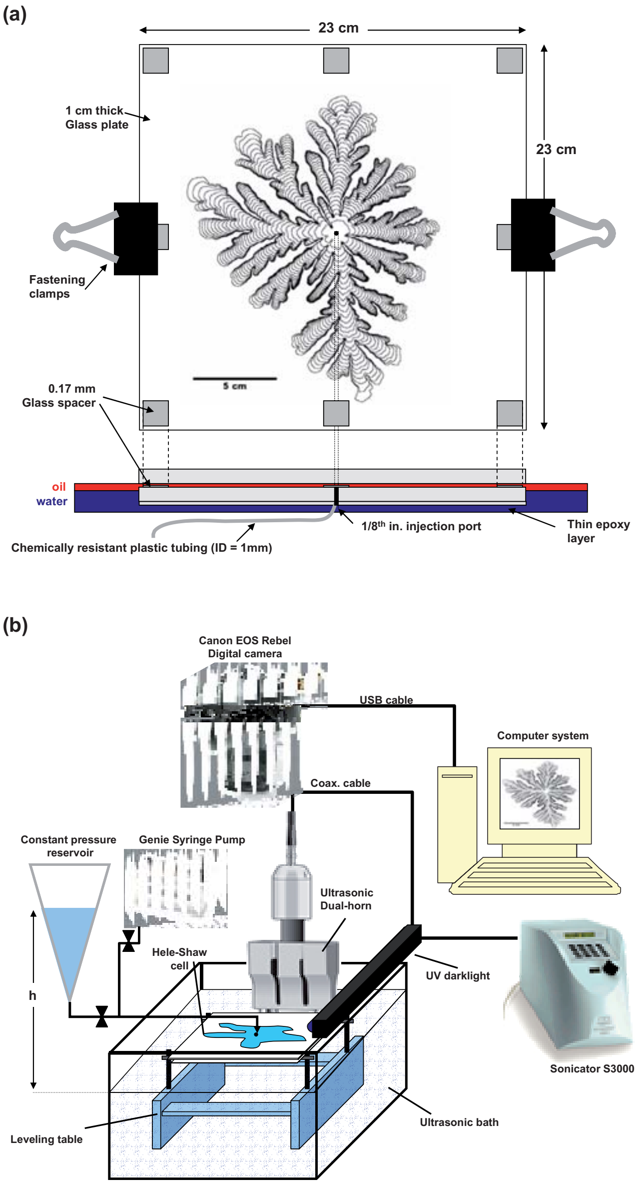

Fig. 1. (a) Hele-Shaw cell and (b) experimental setup.

2 Experimental setup

The experimental setup of all Hele-Shaw experiments is sketched in Figure 1. The Hele-Shaw cell consists of a pair of rectangular glass plates, 23×23 cm^2 wide and 1.0 cm thick, which are separated by eight borosilicate glass spacers approximately $b = 0.17$ mm in height, and 1.5×1.5 cm wide (microscope cover glasses). The glass spacers were glued onto the bottom plate with a 5-min high-adhesion UV-resistant epoxy. To avoid any bending of the glass plates, four additional spacers were introduced on each side. The plates were held together tightly by two fastening clamps. The locations of the spacers are not believed to interfere greatly with the outflow of fluids from the cell, causing minimum disturbance of the pattern front. A white epoxy layer was applied to the bottom plate to provide a white screen, improving the image contrast and facilitating easier image processing. Illumination of the Hele-Shaw cell was accomplished using a standard fluorescent ultraviolet (UV-B) dark light. A syringe pump was used to inject the aqueous phase into a 1/8 in. injection port via a 1 m long chemically resistant vinyl tube. The pump can provid accurate flow rates between 0.001 cc/min and 10 cc/min. For the constant pressure experiments, we used a tear drop glass vessel to maintain a hydrostatic pressure at a precision of around ±0.005 psi. A digital 6.7 mega-pixels camera was installed 0.7 m above the cell, and set to continuously record the injection process at intervals of 10 s.

As an ultrasonic bath, we used a standard 4 gallon tank filled with water. An ultrasonic dual-horn was positioned 15 cm away from the plates to avoid undesired pressure fluctuations at the boundary due to the cavitation zone at the tip, and to minimize vibration of the plates. De-aerated water was used within the bath to minimize the dispersion and absorption of ultrasonic energy due to cavitation, and to facilitate more effective propagation of the sound waves. The Hele-Shaw cell was immersed sufficiently deep into the bath to allow transfer of ultrasonic energy into the liquid. A leveling table was used to horizontally adjust the plates.

The pair of glass plates was carefully cleaned with surfactant, and dried with air and a tissue paper. Then, the active sides were wiped with acetone and water to remove any surfactant on the plates. The plates were then prewetted with a thin film of oil. After a few minutes, the spacers were applied, and the oil was carefully poured evenly onto the plates. Once the mineral oil uniformly spread on the bottom plate, the top plate was slowly applied, and fastened. We also made sure to spread mineral oil along the edges to facilitate a smooth transition of the interface between the fluids within the Hele-Shaw cell and the ultrasonic bath. Great effort was taken to avoid any development of bubbles within the plates or the injection tubing. The saturated plates were then semi-immersed into the ultrasonic bath, and the displacing phase was injected at a constant rate. To reduce the capillary transition between the plates and the bath, we maintained a thin 0.3 cm film of oil above of the bath-water. This film was in direct contact with the annulus between the two plates, and mitigated any sudden jump in the capillary pressure due to the oil-water interface.

Water and 3% DOWFAX 2A1 (Alkyldiphenyloxide Disulfonic Acid: anionic surfactant) were used as the aqueous phase. Both solutions were dyed with water-soluble fluorescent tracer dye (Risk Factor IFWB-C0) that glows under UV darklight to ease subsequent image analysis. DOWFAX 2A1 was used to reduce the interfacial tension allowing a broad range of capillary number. A detailed description of the fluid properties is presented in Tables 1 and 2. For miscible injection, we used two different oleic phases having different miscibility characteristics with heavy mineral oil:

- kerosene (non-volatile)
- heptane (volatile)

These fluids were dyed with an oil soluble fluorescent dye (Risk Factor DFSB-K43) to ease subsequent image analysis.

Table 1. Properties of the fluids used in the experiments (at standard atmospheric conditions). DOWFAX 2A1 = Sodium Dodecyl Diphenyloxide Disulfonate.

Fluid	Density[1] (g/cc)	Viscosity[2] (cp)
Water	0.9982 ± 0.0010	1.0 ± 0.02
Water + 3% DOWFAX 2A1	1.0027 ± 0.0010	5.32 ± 0.27
Light Mineral Oil	0.8383 ± 0.0050	46.5 +0.5
Heavy Mineral Oil	0.8508 ± 0.0050	167.0 + 1.7
Kerosene	0.768 ± 0.0050	2.9 ± 0.03
S60	0.8757 ± 0.0014	141.4 +0.2
S200	0.8876 ± 0.0014	577.9 + 0.9
N350	0.8885 ± 0.0014	1112.0 ± 1.8
S600	0.8913 ± 0.0014	1973.0 +3.2
Heptane	0.6795 ± 0.0010	0.742 ± 0.021

[1] Weight-Volume method using a 5cc syringe

[2] Rotational viscometer (Fann 35A) at 300 rpm; viscosity values for S60, S200, S350 and S600 were obtained from Canon Instrmentation Company (A2AlA Certificate #1262.01)

Table 2. Interfacial tension data for the fluid pairs used in the experiments (at standard atmospheric conditions).

Aqueous Phases	Air and Oleic Phases	Interfacial[1] Tension (dyne/cm)
Water	Light MO	61.8 ±1.2
3% DOWFAX 2A1	Light MO	11.2 ±0.2
Water	Heavy MO	51.0 ± 1.0
3% DOWFAX 2A1	Heavy MO	10.8 ±0.2
Water	Kerosene	40.7 ± 0.8
Water	S60	22.6 ±0.5
Water	S200	30.7 ± 0.6
Water	N350	35.3 ±0.7
Water	S600	38.7 ± 0.8

[1] DuNouy type tensiometer.

Every experiment consists of two runs; one with ultrasound and one without. Experiments were repeated at least three times to ensure repeatability. Each run was evaluated according to the following criteria: (a) repeatability, that was tested by qualitative (visual inspection) and quantitative (fractal dimension–lacunarity comparisons) analysis and (b) radial symmetry. The latter ensures that the growth of fingers is totally controlled by fluid characteristics and ultrasonic effect rather than differences in the Hele-Shaw cell caused by model preparation.

Note, however, that it was not always possible to observe a perfectly radial propagation of the finger front due to the stochastic nature of the flow. This was especially the case with surfactant solution experiments. After each experiment, the resulting images were digitized, and converted into binary images. The fractal dimension (box counting) and lacunarity were estimateed via fractal analysis software (ImageJ FracLac).

3 Fractal analysis

As demonstrated by Paterson [24], viscous fingers can be represented semi-quantitatively by fractal DLA patterns. Given the fractal nature of Hele-Shaw patterns, one may use the fractal dimension to characterize instabilities. Fractal dimension has been employed extensively to quantify the morphology of radial viscous fingering [20,27,29], and is a useful tool to assess its degree of complexity. It defines the scaling rule which dictates the number and scale of new branches. The scaling rule of a fractal is defined by a power-law transformation of scale as

$$N(\varepsilon) = \varepsilon^{-D_B} \tag{5}$$

where N is the minimum number of open sets of diameter ε needed to cover the set [30]. The fractal dimension can be obtained by taking the logarithm of equation (5), rearranging for D_B and taking the limit as ε goes to zero:

$$D_B = \lim_{\varepsilon \to 0} \frac{\log N(\varepsilon)}{\log \varepsilon}. \tag{6}$$

One can attain D_B from box counting by overlaying a binary image onto a grid [31]. For each grid size ε, we count the number of pixels, $N(\varepsilon)$ that is filled with the fingering pattern. Then the best fit to the resulting straight line on a log-log plot gives the fractal dimension.

Besides the fractal dimension, we also employed an additional parameter, namely lacunarity to analyze the displacement patterns. The lacunarity assesses the degree of "gappiness" or "visual texture", and represents the amount of heterogeneity or translational/rotational invariance of a binary image [32]. This measure supplements fractal dimension by introducing a notion of "compactness". A fractal object may have the same fractal dimension, but may display an entirely different texture. At low lacunarity, the fractal is homogeneous, and grows symmetrically and uniformly. As the lacunarity increases, one observes more void space. It is clear that fractal dimension alone is not sufficient as a descriptor of complex patterns. The lacunarity, Λ_ε, is calculated as the variation in pixel density at different ε. First the number of pixels within each grid box of dimension ε is counted using a standard non-overlapping box count. For each ε, a coefficient of variance is computed from the standard deviation (s) and the mean (M) of number of pixels per box:

$$\Lambda_\varepsilon = \left(\frac{s}{M}\right)^2. \tag{7}$$

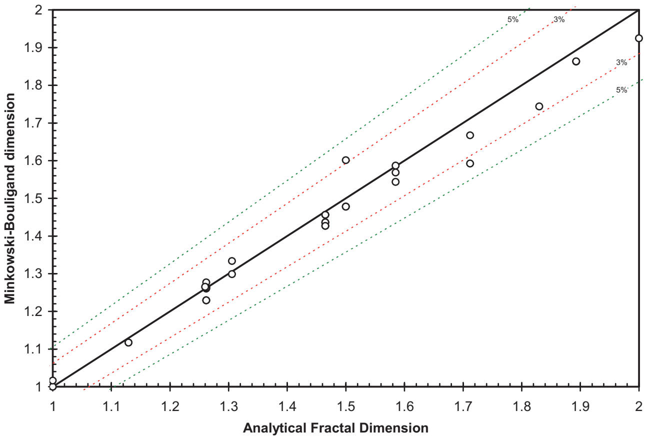

Fig. 2. Cross-comparison plot of the fractal dimensions obtained from FracLac V.2 [33] versus the analytical fractal dimension. The 45^o line corresponds to the case where the computed fractal dimension through box counting equals the analytically determined value. Dashed lines represent the percent deviation from equality.

Thus, the lacunarity is related to the distribution of empty spaces (lacuna) of an image. If an empty region of an image with fractal geometry displays a high diversity of sizes, the lacunarity is usually high. On the other hand, if the fractal is invariant in empty spaces distribution, the lacunarity is low [32]. Since our images have been screened based on their radial symmetry, the fractal lacunarity is only useful in describing finger compactness and empties distribution, and not the rotational invariance.

The open source ImageJ plug-in FracLac V.2.44 [33,34] was used to compute both fractal dimension and the lacunarity of binary images. The source code is readily available online. To test the reliability of the program for 800 × 800 pixel images, we generated a series of analytical fractals using Wolfram Mathematica 5. A cross-comparison plot of analytical fractal dimension versus box counting dimension (Fig. 2) reveals that for most patterns a deviation of less than 3% is expected when using FracLac. Therefore, for a pattern with $D_B = 1.5$ we anticipate a nominal error of ± 0.045. It was also shown by Karperien [33] that FracLac performs especially well on contours and fractal outlines.

After the validation of the software package used for fractal analysis, we measured the fractal (box counting) dimensions and lacunarity of the fingering images. Figure 3 shows the fractal plot as grid size (ε in Eq. (1)) vs. the number of box counts ($N(\varepsilon)$ in Eq. (1)) to obtain D_B. The results show that the images follow a fractal behavior for about a decade indicated by a straight line. As the grid size increases, a deviation from the straight line with increased fluctuations is observed. The fractal plot for the fingering patterns of the largest subset, that corresponds to the mature stage of the experiments, is shown in Figure 4. One can observe that they all show a fractal trend and differences are mainly due to the nature of the fluid pairs and ultrasonic effect.

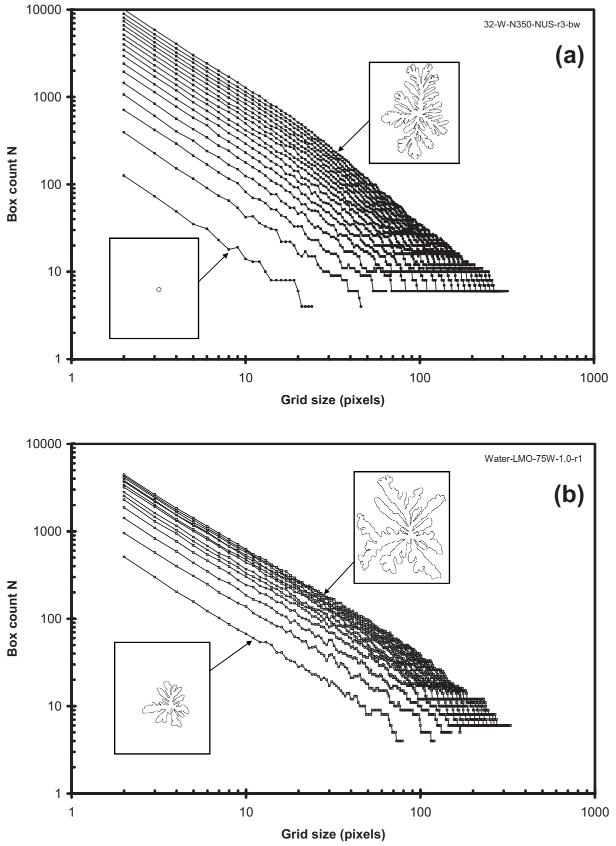

Fig. 3. Box count plots of selected visous finger patterns at several stages of formation: (a) water-oil type N350 (no ultrasound), and (b) water-LMO (75W ultrasound) pairs.

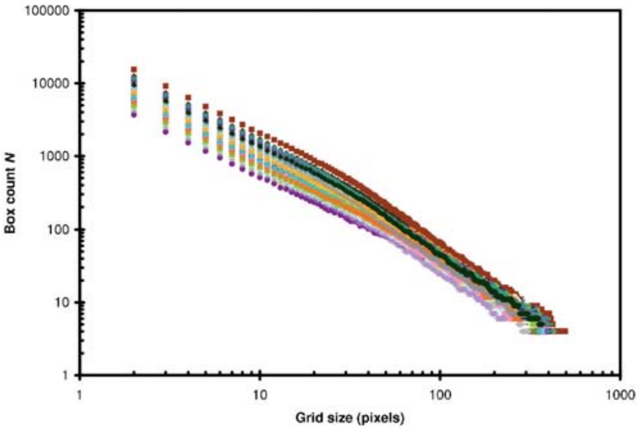

Fig. 4. Box count plots for all patterns at the mature stage (the largest subset).

A similar analysis was done for lacunarity (Fig. 5). The two plots in this figure show that the error involved is very minimal for smaller box sizes and does not exceed 1% for as the grid sizes becomes larger. In the subsequent analysis, "lacunarity with empties" corresponds to the average value of the lacunarity box count curve.

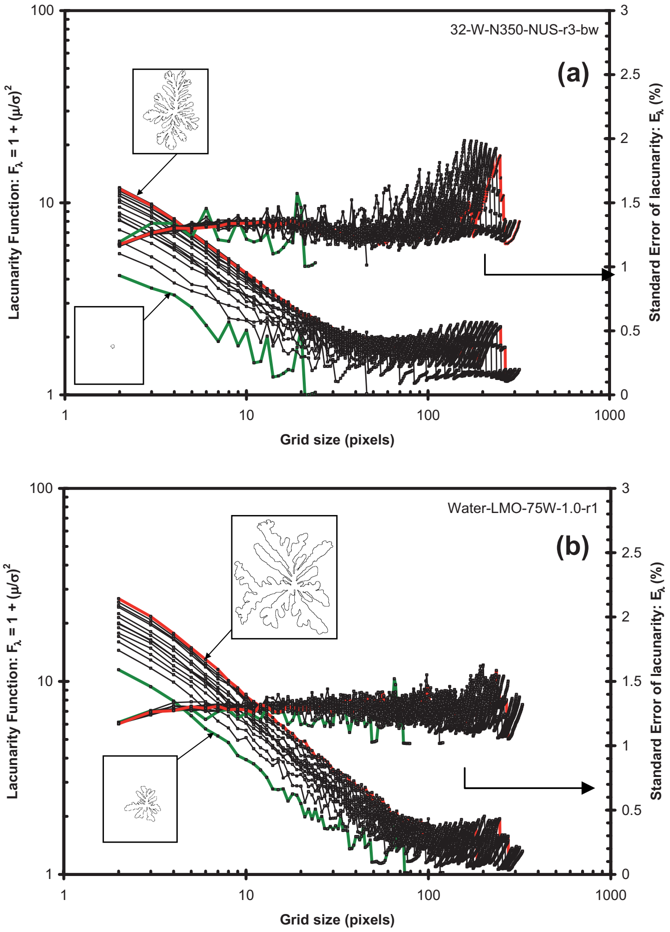

Fig. 5. Lacunarity plots for the evolving fingering images until it reaches the maturity stage (the largest subset) for (a) water-oil type N350 (no ultrasound), and (b) water-LMO (75W ultrasound).

4 Results and discussion

4.1 Immiscible Hele-Shaw experiments

4.1.1 Constant rate water

Immiscible fingering patterns developed during constant injection of water to displace heavy mineral oil are shown in Figure 6. All patterns have been scaled so that each tick mark represents 0.5 cm in real scale. Due to space constraints, we will only present the composite contour plots. Each contour outlines the state of the liquid-liquid interface as it evolves through time at 10 s intervals. Two qualitative features may be extracted visually from the contour composites: (a) the curvature of the interface, and (b) the direction of interface propagation. In some cases, the interface does not only propagate radially outward from the injection port, but also expands laterally. This type of flow is easily distinguished by darkening the outline around the viscous fingers.

Figure 6a shows the fractal pattern generated after injecting water into heavy mineral oil at a constant injection rate of 0.3 cm^3/min. The viscosity ratio is 166.7 ± 1.7 and

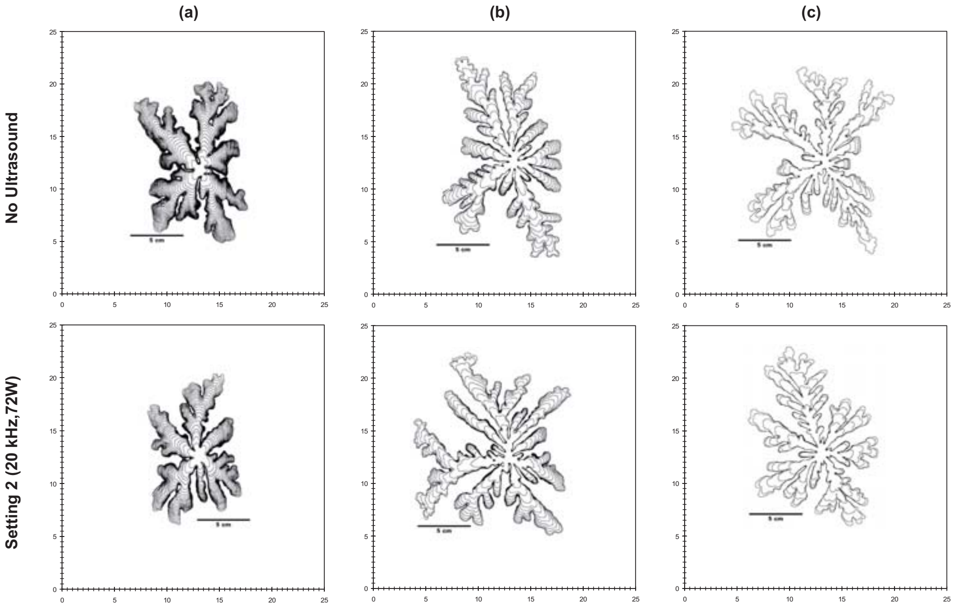

Fig. 6. Immiscible Hele-Shaw patterns for water injected into heavy mineral oil at constant rates of (a) 0.3 cc/min, (b) 1.0 cc/min, and (c) 2.0 cc/min. The scale of all images is in centimeters. The contours represent the location of the interface at 10 second intervals. $\mu_O = 167.0 \pm 1.7$ cp; IFT $= 51.0 \pm 1.0$ dynes/cm.

the interfacial tension is 51 ± 1 dynes/cm. There is a clear difference between the patterns obtained with and without ultrasonic effect. With no ultrasonic energy applied, we observed the formation of six major branches with only small secondary branches. The curvature of the contours is relatively low, with tips gradually flattening as the pattern matures. Substantial thickening of the branches was also characteristic to this viscosity ratio. On the other hand, the ultrasonically stimulated pattern displayed thinner primary fingers, and longer secondary branches. The curvature of the interface was high at early times, and also flattened as the pattern matured. Branch thickening was suppressed, and the fingers primarily advanced at the tips.

As we stepped up to consecutively higher injection rates, we observed a similar, but less severe response to ultrasonic energy compared to the low rate case. Figure 6b displays the contour development after injecting water into heavy mineral oil at 1 cm^3/min. Again, the ultrasonic pattern was more compact exhibiting more uniform branching, and thicker and smoother fingers. After applying ultrasound, we noted that the branches have more erratic secondary divisions. It is apparent that ultrasound induced a more stable front, resulting in longer primary fingers and suppressed secondary fingering. In other words, the low curvature flanks of the fingers were stabilized whereas the high curvature tips were not. After raising the injection rate to 2.0 cm^3/min (Fig. 6c), the patterns exhibited similar branching behavior with secondary branching occurring at regular intervals for both ultrasonic and no-ultrasonic cases.

Figures 7a and 7b present the box counting fractal dimension and lacunarity change against time for the patterns shown in Figure 6. These plots illustrate the consistent linear growth of the pattern. They also serve to

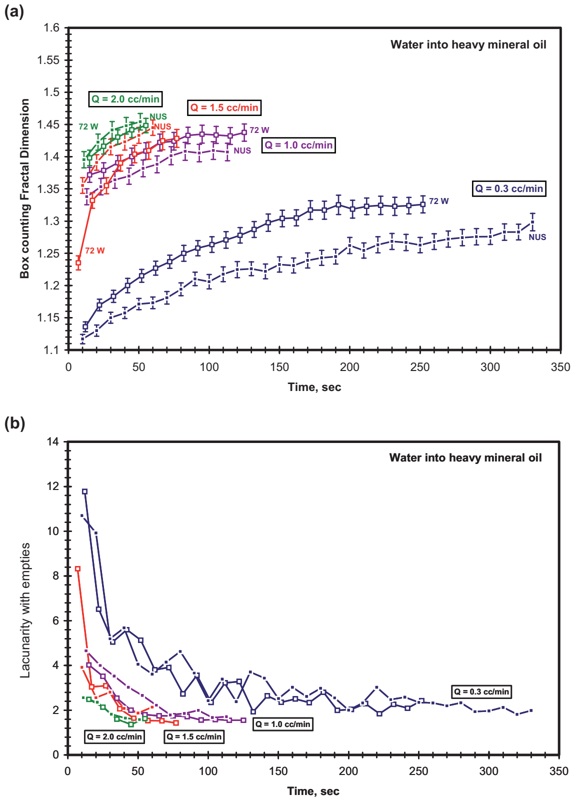

Fig. 7. (a) Fractal dimension and (b) lacunarity as a function of time for water into heavy mineral oil (HMO) at four constant injection rates: 0.3, 1.0, 1.5, and 2.0 cc/min. The viscosity and interfacial tension of HMO is 167.0 ± 1.7 cp and 51.0 ± 1.0 dynes/cm, respectively. Patterns for 0.3, 1.0, and 2.0 cc/min are shown in Figure 3. Solid points represent the case without ultrasound, and empty points with 72W, 20 kHz ultrasound.

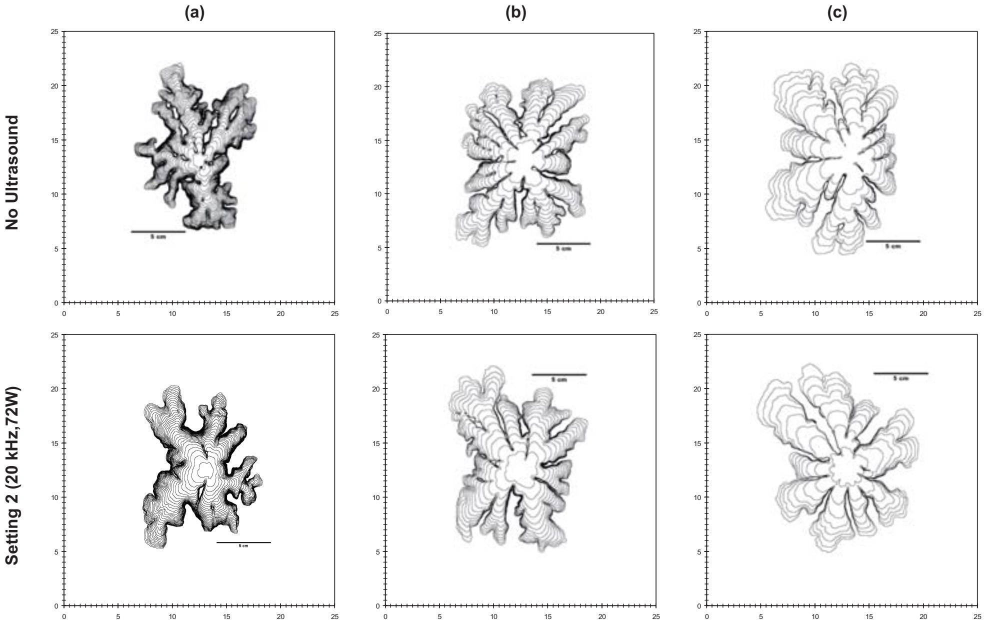

Fig. 8. Immiscible Hele-Shaw patterns for water injected into light mineral oil at constant rates of (a) 0.3 cc/min, (b) 1.0 cc/min, and (c) 2.0 cc/min. The scale of all images is in centimeters. The contours represent the location of the interface at 10 second intervals. $\mu_O = 46.5 \pm 0.5$ cp; IFT $= 61.8 \pm 1.2$ dynes/cm.

demonstrate the consistency and repeatability of our experiments, and the reliability of our image processing method. In all cases, ultrasound enhanced the length of the perimeter of the fractal pattern, but did not noticeably affect the areal growth. The plot of fractal dimension vs. time (Fig. 7a) clearly shows that ultrasound stabilizes the front, and that it reduces the level of instability at the interface. Visually, this is reflected as a reduction in branching, and more primary fingers. For injection rates below 1.5 cm^3/min, the ultrasonic patterns assume considerably higher fractal dimension. The difference in the fractal dimensions between ultrasound and no-ultrasound cases becomes smaller with increasing injection rate. Based on this observation, one can conclude that the effect of ultrasound on the fingering patterns is less pronounced as the viscous forces start dominating the displacement.

In the case of lighter mineral oil (LMO), the effect of ultrasound on the patterns was more distinguishable and differed considerably comared to the heavy mineral oil case. Figure 8a shows the resulting patterns after injecting water into light mineral oil at 0.3 cm^3/min. Unlike with heavy mineral oil, ultrasonic stimulation resulted in patterns with thicker, more pronounced primary branches, and a significant reduction in secondary branching. No-ultrasound cases exhibited thinner primary branches with more secondary branches. This is reflected in a significant drop in fractal dimension (Fig. 9). The same reduction in fractal dimension was noticed at an injection rate of 1.0 cm^3/min (Fig. 9). At higher rates (1.5 cm^3/min and 2.0 cm^3/min), the difference in fractal dimension between ultrasound and no-ultrasound cases decreased considerably in consistent with the heavy mineral oil case.

Based on these findings, we extended our analysis by plotting fractal dimension against the modified capillary number. The results for both light and heavy mineral oil cases are shown in Figure 10a. This plot shows the relationship between the fractal dimensions and the modified capillary number after 10, 50, 100 and 200 s. As seen, the fractal dimension continuously increases as the pattern evolves and more branching occurs, until it stabilizes at a characteristic fractal dimension. For the heavy mineral oil case, the characteristic fractal dimension is approximately 1.55, while for the light mineral oil, it is 1.42.

Although light mineral oil shows slightly lower fractal dimension at ${N_{\text{Ca}}}' = 400$, the curves are relatively well connected, and hint towards a logarithmic trend. At low capillary numbers (${N_{\text{Ca}}}' < 250$), we observed a steep decline in fractal dimension, ranging between 1.05 to 1.45. At higher capillary numbers (${N_{\text{Ca}}}' > 300$), the fractal dimension stabilizes at a constant value that depends on the oleic phase viscosity. To illustrate the contribution due to ultrasound, we also plot the difference in fractal dimension obtained with and without ultrasound (Fig. 10b). Note that for heavy mineral oil, ultrasound increases the fractal dimension at low capillary number (up to 7%), but declines at high capillary numbers (up to 3%). The opposite occurs with the light mineral oil.

4.1.2 Constant pressure water

Until now, we only discussed the effect of ultrasound at constant injection of water. This scenario is intrinsically forced and dominated by viscous forces. It is therefore necessary to also perform a series of Hele-Shaw experiments at constant pressure injection. This process is dictated by the system, i.e. injectivity depends on the mobility of the oil within the Hele-Shaw cell. Given the same injection

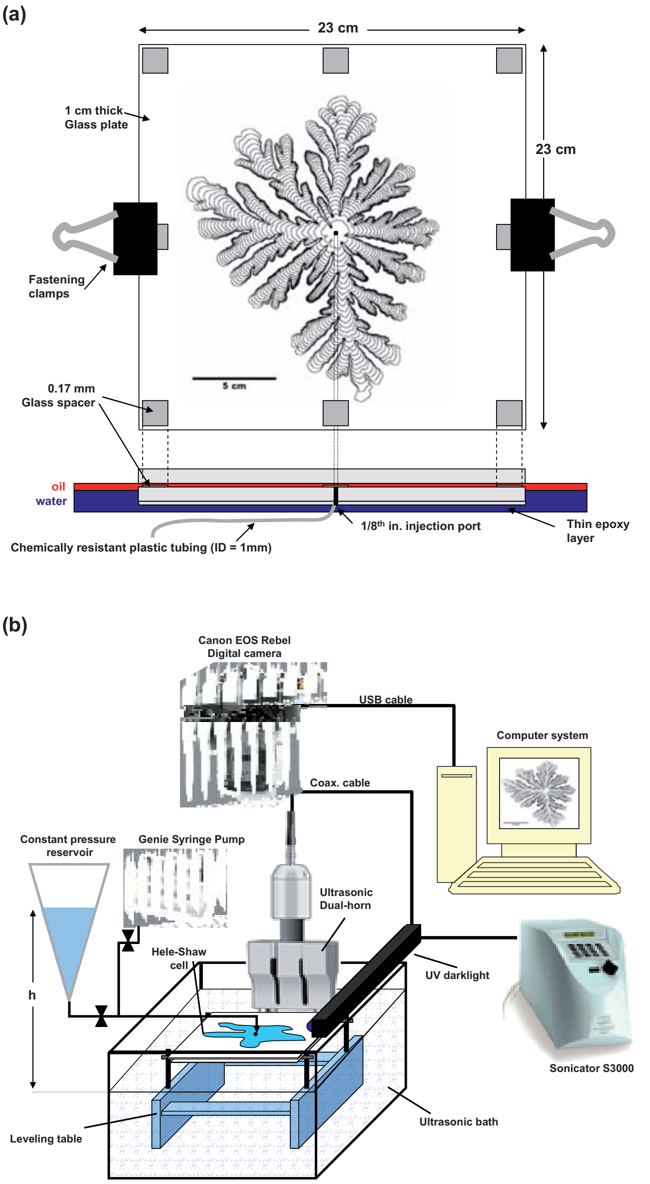

Fig. 9. Fractal dimension as a function of time for water into light mineral oil (LMO) at four constant injection rates: 0.3, 1.0, 1.5, and 2.0 cc/min. The viscosity and interfacial tension of LMO is 46.5 ± 0.5 cp and 61.8 ± 1.2, respectively. Patterns for 0.3, 1.0, and 2.0 cc/min are shown in Figure 6. Solid points represent the case without ultrasound, and empty points with 72W, 20 kHz ultrasound.

pressure, injectivity is lower for high viscosity oil than for low viscosity oil, and thus, one would expect patterns with reduced branching.

Figure 11a through f show the resulting patterns after injecting water at a constant pressure of 0.455 psi (and 0.9947 psi in (f)) into a Hele-Shaw cell saturated with five types of processed mineral oils. These oils, designed to yield accurate, consistent viscosity readings, and are used to calibrate high precision viscometers, were selected to cover a broad range of viscosity values. The physicochemical properties of all fluids are given in Tables 1 and 2.

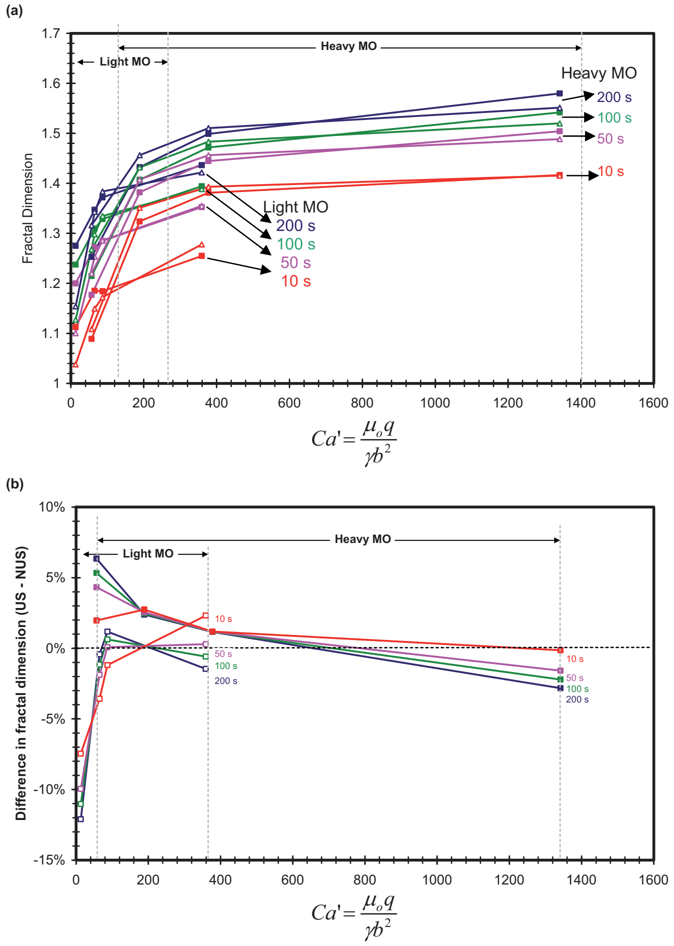

Fig. 10. (a) Fractal dimension versus modified capillary number for light mineral oil and heavy mineral oil at different times of pattern formation. (b) Difference in fractal dimension for light and heavy mineral oil versus modified capillary number.

Although it is very difficult to discern any differences visually, ultrasound did increase the fractal dimension of the pattern. A significant increase in lacunarity was observed at early times only. Figure 11b provides contour composite plots after using S60 ($\mu_o = 141.4 \pm 0.2$, IFT $= 22.6 \pm 0.5$ dynes/cm) as the viscous fluid. S60 has similar viscosity as heavy mineral oil, but half the interfacial tension. We noted that the reduction in interfacial tension (and therefore, the capillary number) cause a dramatic increase in fractal dimension at high ultrasonic intensity. Figure 11c shows the fractal patterns for S200 oil ($\mu_o = 577.9 \pm 0.9$, IFT $= 30.7 \pm 0.6$ dynes/cm). The fractal perimeter and area decrease remarkably with intermediate intensity ultrasound, while it did not show much response at high intensity. This may not necessarily be due to ultrasound, but possibly an artifact of the box counting method. The fractal dimension and lacunarity did not yield a noteworthy change with ultrasound. As can be seen in Figure 11d, a similar response may be noted with N350 ($\mu_o = 1112.0 \pm 1.8$ cp, IFT $= 35.3 \pm 0.8$ dynes/cm) for ultrasound and no-ultrasound cases. Finally, we investigated the effect of ultrasound on very high viscosity oil,

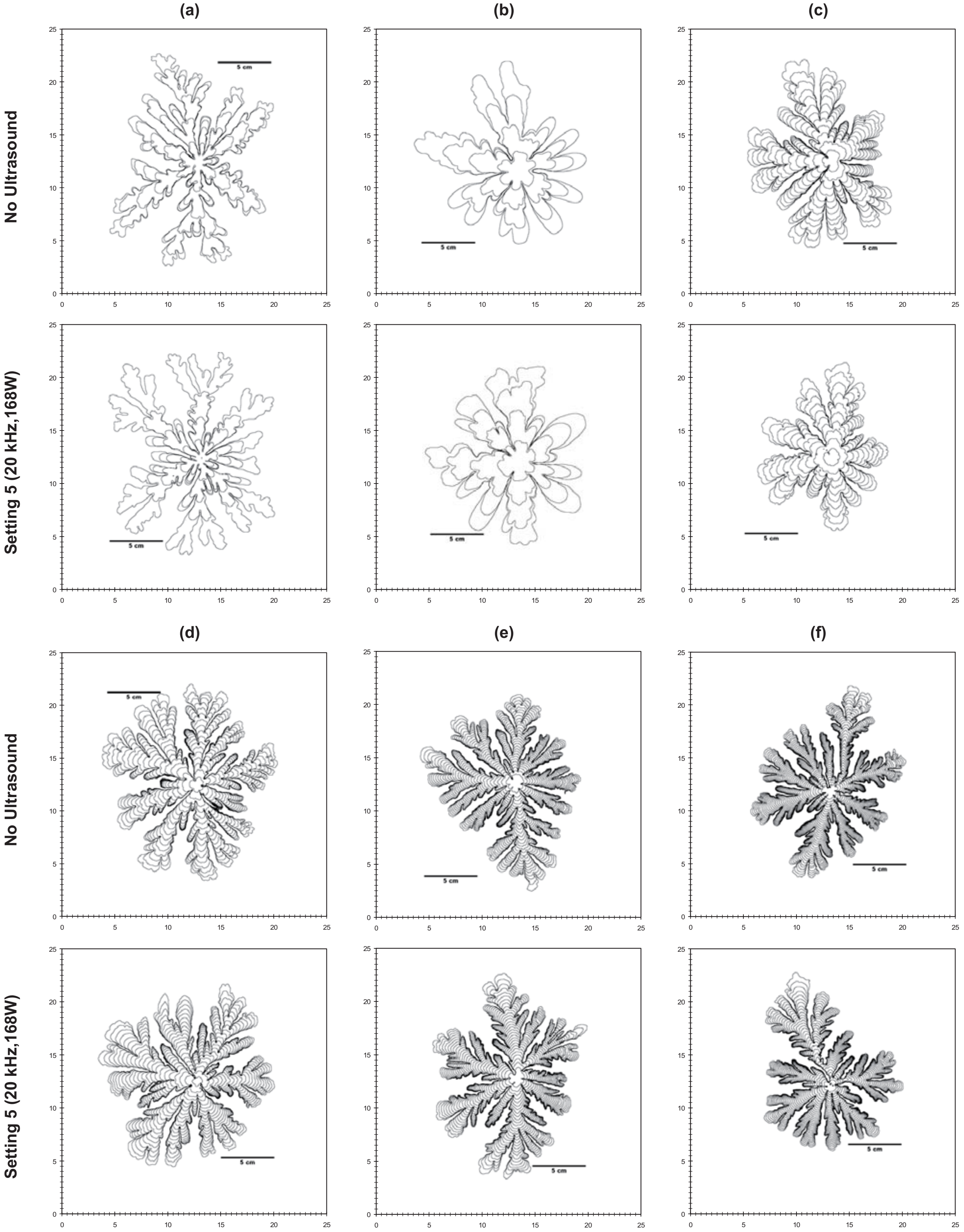

Fig. 11. Immiscible Hele-Shaw patterns for water injected into (a) heavy mineral oil (0.455 psi), (b) S60 (0.455 psi), (c) S200 (0.455 psi), (d) N350 (0.455 psi), (e) S600 (0.455 psi) and (f) S600 (0.9947 psi) at a constant head pressure. The viscosity and interfacial tension of S600 is 1973 ± 3.2 cp and 38.7 ± 0.8 dynes/cm, respectively. The scale is in centimeters. The contours represent the location of the interface at 10 s intervals.

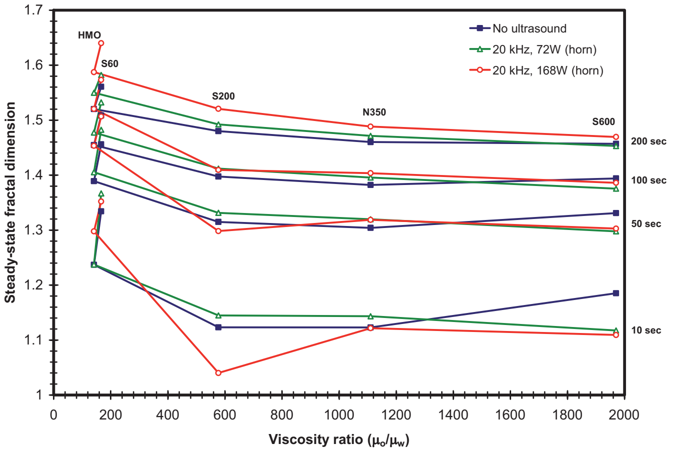

Fig. 12. Steady state fractal dimension (from logarithmic fit fitted) versus viscosity ratio for various processed mineral oils.

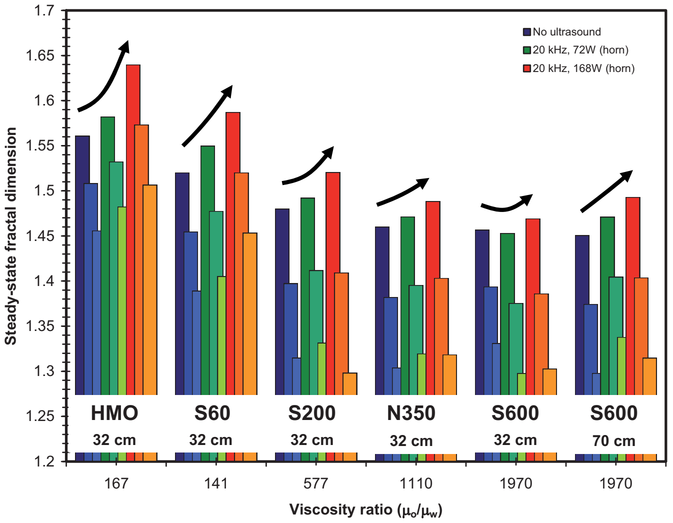

Fig. 13. Bar chart illustrating the relative change (arrows) of fractal dimension for each processed oil. Each "sub-bar" indicates the fractal dimension at 50, 100 and 200 s. The bars with the highest fractal dimension represent the fractal dimension at 200 s (point where the fractal dimension has a stabilized value).

S600 ($\mu_o = 1973 \pm 3.2$ cp, IFT $= 38.7 \pm 0.8$ dynes/cm), and found that regardless of pressure, the fractal perimeter, area and fractal dimension did not react significantly to ultrasonic energy.

Figure 12 summarizes the fractal analysis for those different oil viscosity cases. It shows the change in fractal dimension (obtained after the fractal dimension reaches an almost constant value over time) with viscosity ratio at various stages of pattern development. The switch between heavy mineral oil (HMO) and S60 may be due to the reduction in interfacial tension. In all cases, the fractal dimension decreases with increasing viscosity ratio, and increases with time. Additionally, the difference between the fractal dimension from ultrasonically stimulated patterns and those without ultrasound decreases with increasing viscosity ratio. Therefore, ultrasound effectively perturbs the interface when the viscosity ratio between aqueous phase and the oil is low.

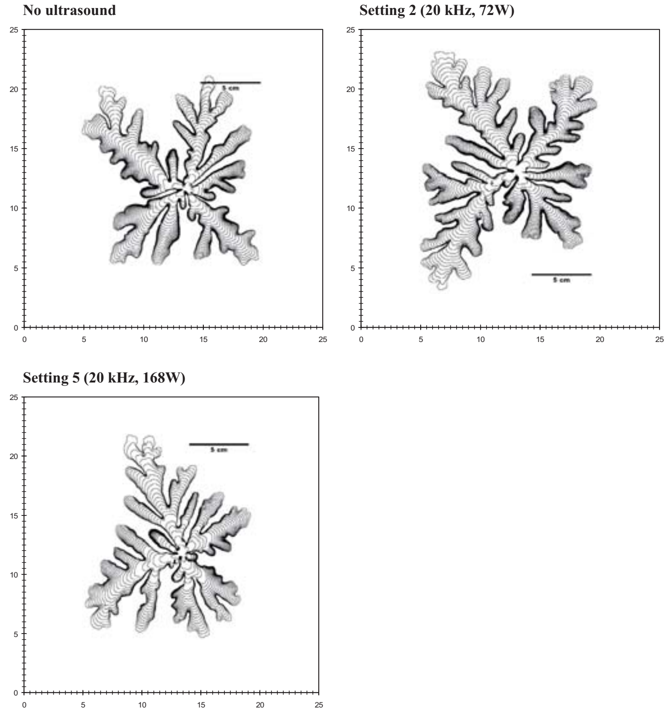

Fig. 14. Immiscible Hele-Shaw patterns for 3% DOWFAX 2A1 injected into heavy mineral oil (HMO) at a constant head pressure of 0.1421 psi. The viscosity and interfacial tension of HMO is 167.0 ± 1.7 cp and 51.0 ± 1.0 dynes/cm, respectively. The scale is in centimeters. The contours represent the location of the interface at 10 s intervals.

Figure 13 shows a histogram of steady state fractal dimension with increasing viscosity ratio. Each set of three bars indicates the fractal dimension at progressively smaller time steps: i.e. dark blue indicates the fractal dimension at 200 seconds, while light blue at 50 s. Arrows illustrate the trend as the ultrasonic intensity is raised from 0 to 169 W. The "slope of the arrows" gradually decreases with increasing viscosity ratio, except for the last case, where we increased the injection pressure from 0.455 psi to 0.9947 psi.

4.1.3 Constant pressure: surfactant solution (3% DOWFAX 2A1)

Because of the observed difference in fractal behavior between HMO and S60 (two oils having very close viscosities but remarkably different interfacial tensions) at constant pressure, we decided to run a series of Hele-Shaw experiments at reduced interfacial tension by adding 3 wt% DOWFAX 2A1 to water. Figures 14–16 show the resulting fractal patterns after 3 wt% DOWFAX 2A1 solution is injected to displace heavy mineral oil at three injection pressures: 0.1421 psi, 0.2373 psi, and 0.357 psi. With the exception of the 0.2373 psi case, fractal dimension and lacunarity remained unaffected (Fig. 17). Again, the high

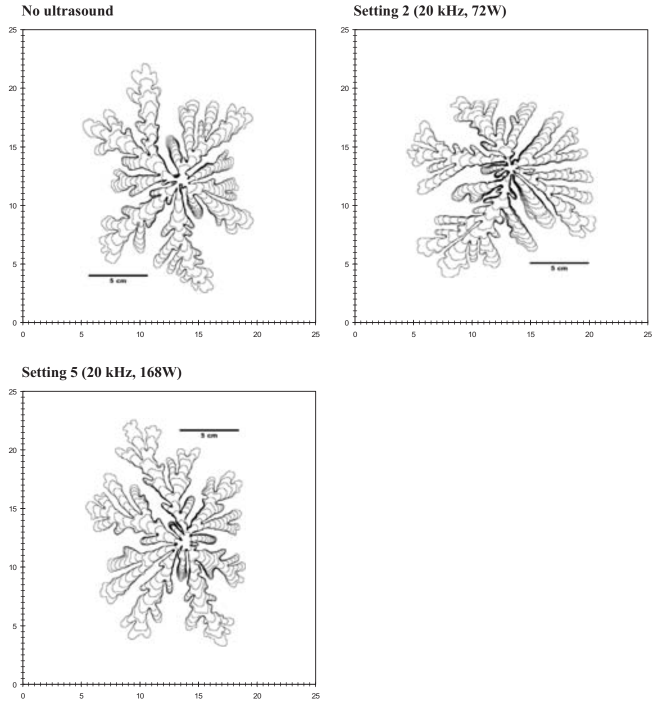

Fig. 15. Immiscible Hele-Shaw patterns for 3% DOWFAX 2A1 injected into heavy mineral oil (HMO) at a constant head pressure of 0.2373 psi. The viscosity and interfacial tension of HMO is 167.0 ± 1.7 cp and 51.0 ± 1.0 dynes/cm, respectively. The scale is in centimeters. The contours represent the location of the interface at 10 s intervals.

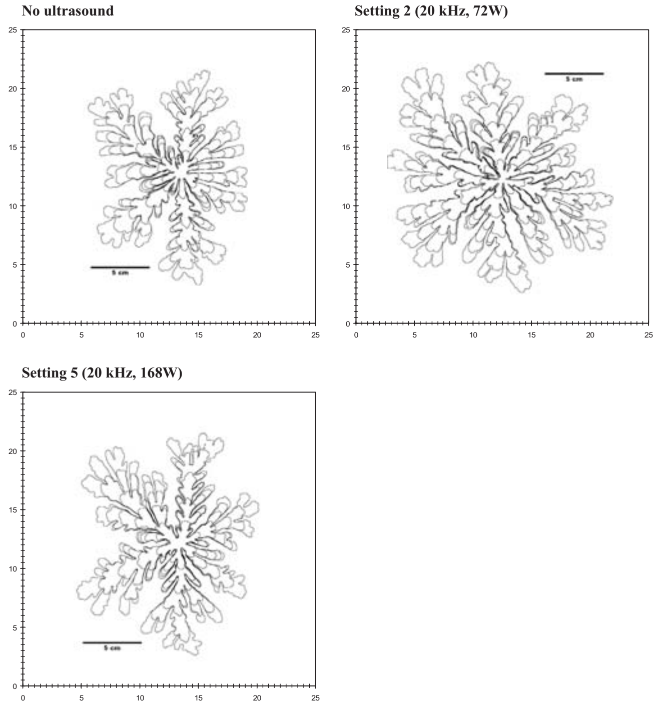

Fig. 16. Immiscible Hele-Shaw patterns for 3% DOWFAX 2A1 injected into heavy mineral oil (HMO) at a constant head pressure of 0.357 psi. The viscosity and interfacial tension of HMO is 167.0 ± 1.7 cp and 51.0 ± 1.0 dynes/cm, respectively. The scale is in centimeters. The contours represent the location of the interface at 10 s intervals.

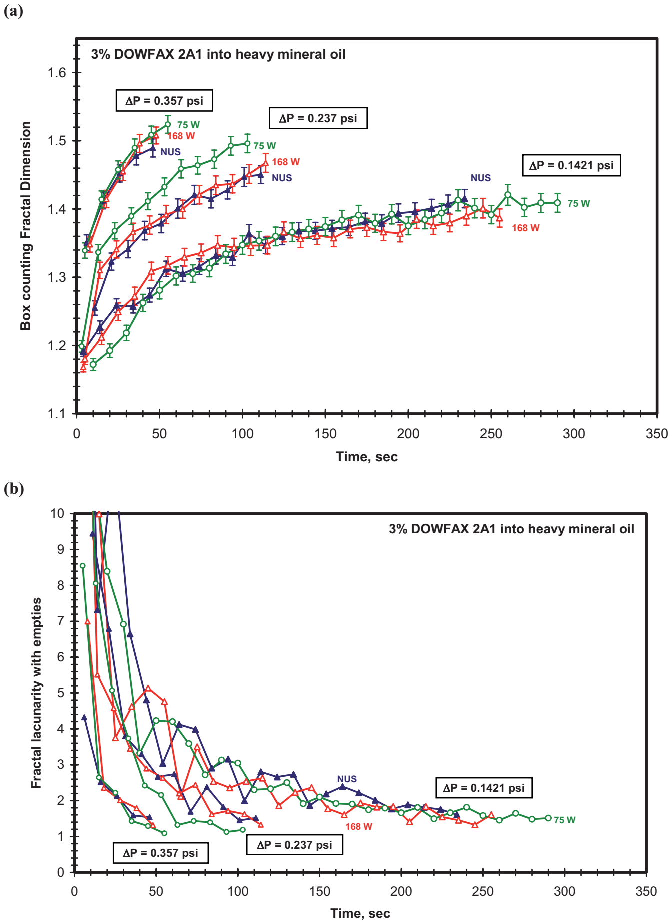

Fig. 17. (a) Fractal dimension and (b) fractal lacunarity as a function of time for 3% DOWFAX 2A1 into heavy mineral oil (HMO) at two constant injection pressures: 0.1421 psi and 0.235 psi. The viscosity and interfacial tension of HMO (with surfactant) is 167.0 ± 1.7 cp and 10.8 ± 0.2 dynes/cm, respectively. Patterns are shown in Figures 12 to 14.

viscosity of the heavy mineral oil reduced the efficacy of ultrasound.

Experiments with light mineral oil yielded more promising results. Figures 18 and 19 show the injection profiles of 3 wt% DOWFAX 2A1 into light mineral oil at two injection pressures: 0.1421 and 0.235 psi, respectively. The response to ultrasound was more remarkable for the case of 0.1421 psi as reflected in the fractal plot (Fig. 20a). Increasing the intensity of ultrasound reduced the fractal dimension of the pattern dramatically but the lacunarity was unaffected (Fig. 20b).

4.2 Miscible Hele-Shaw experiments

To investigate the fingering behavior of miscible floods in Hele-Shaw cells under ultrasound, we injected kerosene (non-volatile) and heptane (volatile) at a constant pressure into light and heavy mineral oil. During a miscible flood, the interfacial tension is zero, and the process is entirely viscosity dominated. Therefore, these experiments

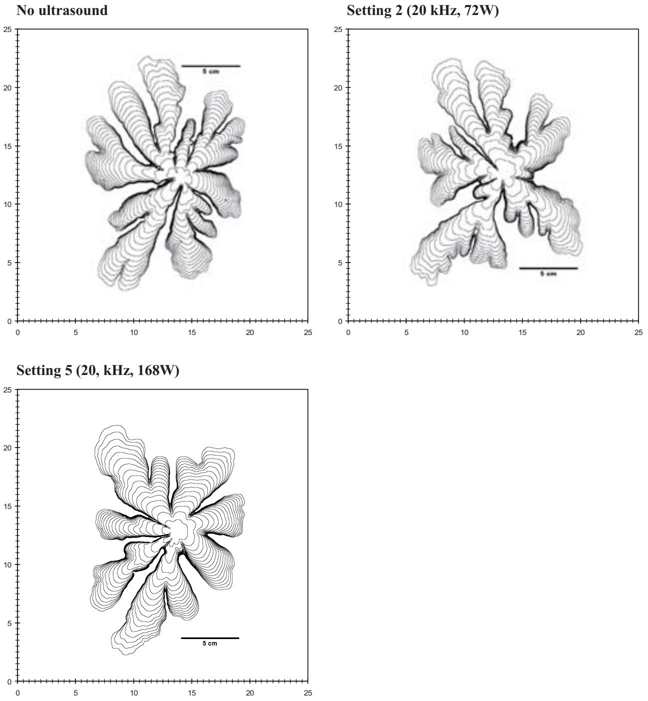
No ultrasound

Setting 2 (20 kHz, 72W)

Setting 5 (20, kHz, 168W)

Fig. 18. Immiscible Hele-Shaw patterns for 3% DOWFAX 2A1 injected into light mineral oil (LMO) at a constant head pressure of 0.1421 psi. The viscosity and interfacial tension of LMO is 46.5 ± 0.5 cp and 61.8 ± 1.2 dynes/cm, respectively. The scale is in centimeters. The contours represent the location of the interface at 10 s intervals.

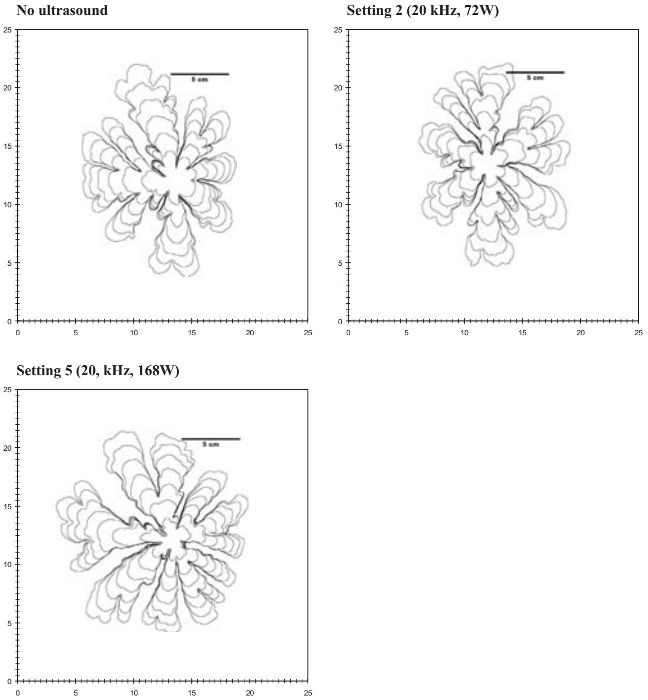
No ultrasound

Setting 2 (20 kHz, 72W)

Setting 5 (20, kHz, 168W)

Fig. 19. Immiscible Hele-Shaw patterns for 3% DOWFAX 2A1 injected into light mineral oil (LMO) at a constant head pressure of 0.235 psi. The viscosity and interfacial tension of LMO is 46.5 ± 0.5 cp and 61.8 ± 1.2 dynes/cm, respectively. The scale is in centimeters. The contours represent the location of the interface at 10 s intervals.

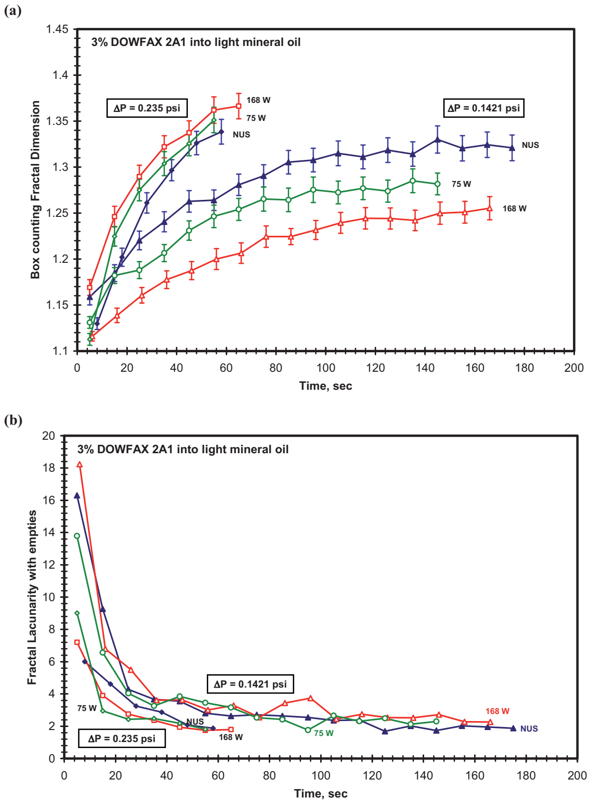

Fig. 20. (a) Fractal dimension and (b) fractal lacunarity as a function of time for 3% DOWFAX 2A1 into light mineral oil (LMO) at two constant injection pressures: 0.1421 psi and 0.235 psi. The viscosity and interfacial tension of LMO is 46.5 ± 0.5 cp and 11.2 ± 0.2 dynes/cm, respectively. Patterns are shown in Figures 17 and 18.

provide valuable insight into viscous displacement processes while entirely eliminating complexities associated with the interfacial forces.

Figure 21 shows various injection profiles for kerosene injection to displace heavy (Fig. 21a) and light mineral oil (Fig. 21b) at a constant head of 9.5 cm. The viscosity ratio of kerosene to light and heavy mineral oil is 16 and 57.6, respectively. Patterns are shown for two intensities of ultrasound, and are labeled as 72 W (setting 2) and 168 W (setting 5). One can clearly see that in the absence of interfacial forces, the displacement front is perfectly circular. In the case when kerosene displaces heavy mineral oil (Fig. 21a), the ultrasound dramatically increased both the length of the fingers, as well as the spacing. Without ultrasound, the injection profile is compact, with a large circular mixing zone at the center. As the ultrasonic intensity is increased, the central mixing zone becomes gradually smaller, and the fingers become longer, and more branched. At high intensity, both primary and secondary branches are long, and the central mixing zone is relatively small. The mixing zone at the finger tips is not noticeably affected by ultrasound.

The patterns observed with light mineral oil exhibited an entirely different behavior (Fig. 21b). Ultrasound reduced the number of secondary branches at the tip, and

(a) Kerosene into heavy mineral oil; Pressure head: 9.5 cm

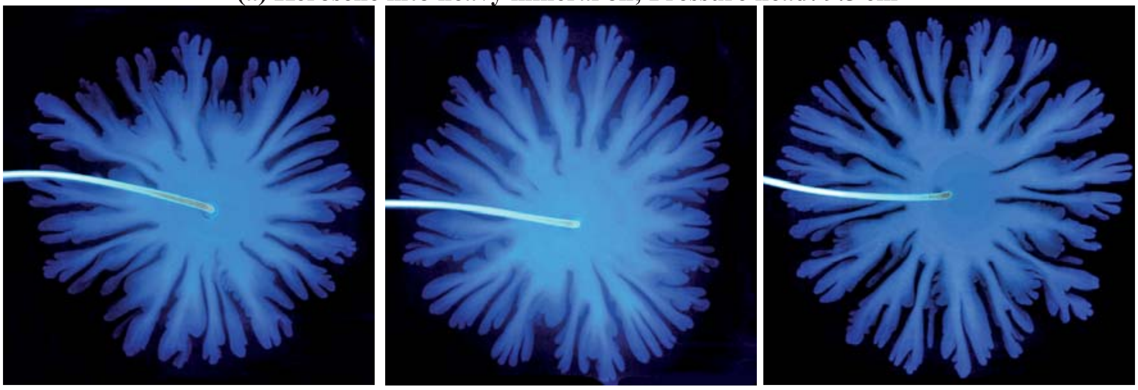

NUS **72 W** **168 W**

(b) Kerosene into light mineral oil; Pressure head: 9.5 cm

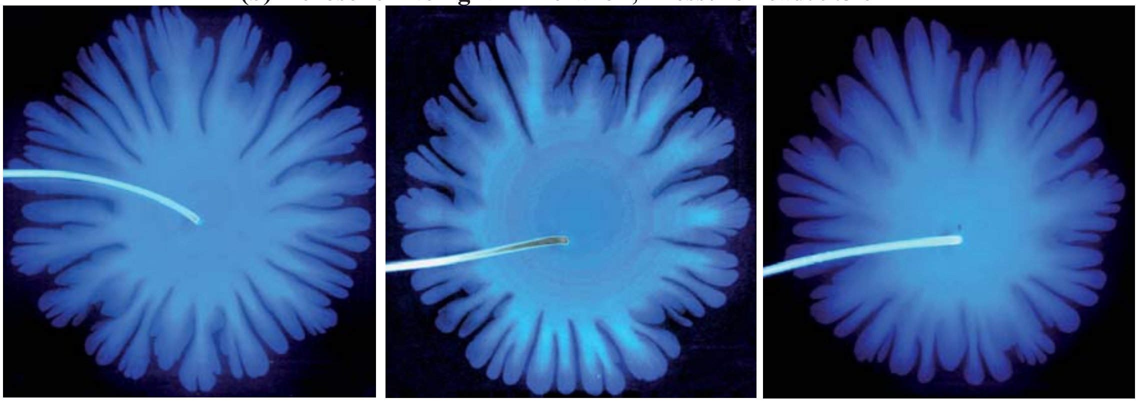

NUS **72 W** **168 W**

Fig. 21. Injection profiles of miscible Hele-Shaw experiments, in which kerosene is injected at a constant head of 9.5 cm into (a) heavy mineral oil ($\mu_{\rm HMO}/\mu_K = 57.6$) and (b) light mineral oil ($\mu_{\rm LMO}/\mu_K = 16.0$). Two intensities of ultrasound (setting 2 = 72 W, setting 5 = 168 W) were applied to the cells. Patterns are compared to the no-ultrasound case (NUS).

yielded an extremely diffuse mixing zone at the center of the pattern, as well as at the primary fingers. The pattern at intermediate intensities showed short primary fingers, and thick secondary fingers which branched out radially.

When the hydrostatic head was raised to 20 cm, we did not notice any dramatic change in finger properties for the heavy oil (Fig. 22a). We, however, observed a change in finger thickness with light mineral oil (Fig. 22b). It is apparent that ultrasound is more effective at low injection pressures, and low viscosity ratios. The diffusivity constants of both fluids may also play a key role in our observations and this could be further investigated.

Injecting heptane into light mineral oil resulted in an extraordinary change in branching behavior. Figure 23 shows the injection profiles for heptane displacing light mineral oil at a constant hydrostatic head of 3 cm. It can be seen that the primary branches visibly longer after ultrasound, and that the pattern is less compact than without ultrasound. The diffusive mixing zone, however, seems to be suppressed at the finger tips and at the center of the pattern.

Raising the hydrostatic head to 5 cm resulted in a similar behavior as observed with kerosene. For both light and heavy mineral oil cases (Fig. 24), the length and width of the primary and secondary branches increased with higher intensity. We observed a substantial improvement in diffusivity at the mixing zone under ultrasound, especially the regions around the finger tips. A similar observation was also made when the hydrostatic head is raised to 9.5 cm.

5 Conclusions and remarks

A series of immiscible and miscible Hele-Shaw experiments were run to investigate the formation of ultrasonically induced instabilities at the liquid-liquid interface. Fractal analysis methods were employed, and proved to be helpful in assessing the effects of ultrasonic waves on immiscible and miscible displacement in porous media. Experiments were conducted to test a broad range of viscosity ratios and interfacial tension. An anionic surfactant was employed to lower the interfacial tension between the injected fluid and the viscous fluid within the Hele-Shaw cell.

We observed that in the case of constant rate water injection into heavy oil, the fractal dimension increased with ultrasound, but remained unchanged at high injection rates. The opposite was true for light mineral oil.

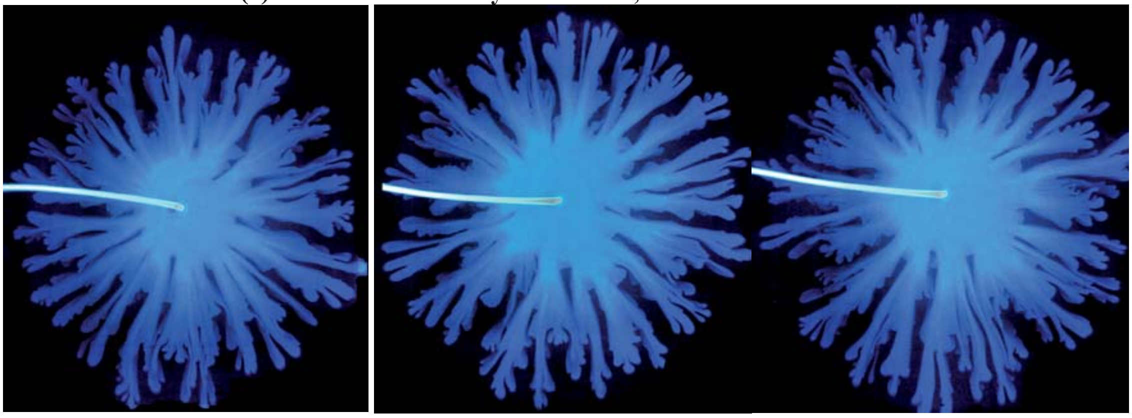
(a) Kerosene into heavy mineral oil; Pressure head: 20 cm

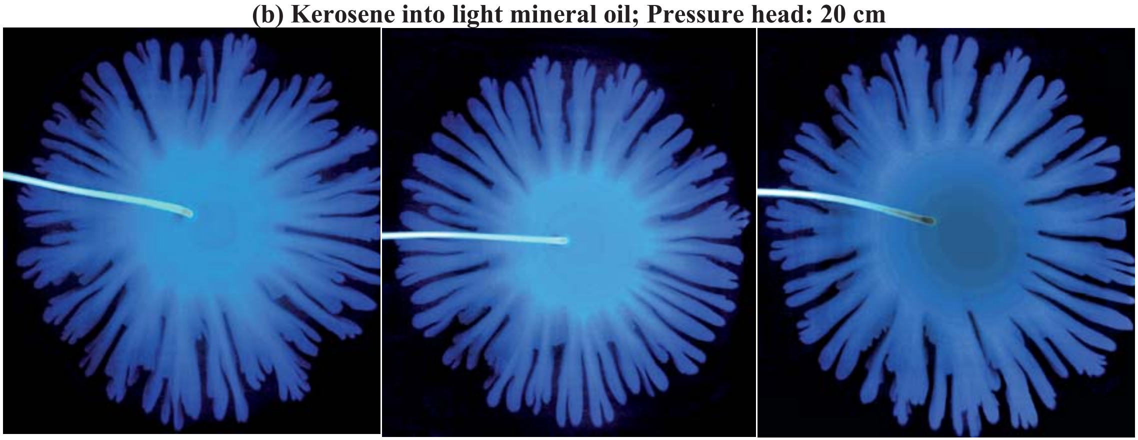
(b) Kerosene into light mineral oil; Pressure head: 20 cm

Fig. 22. Injection profiles of miscible Hele-Shaw experiments, in which kerosene is injected at a constant head of 20 cm into (a) heavy mineral oil ($\mu_{\text{HMO}}/\mu_K = 57.6$) and (b) light mineral oil ($\mu_{\text{LMO}}/\mu_K = 16.0$). Two intensities of ultrasound (setting $2 = 72$ W, setting $5 = 168$ W) were applied to the cells. Patterns are compared to the no-ultrasound case (NUS).

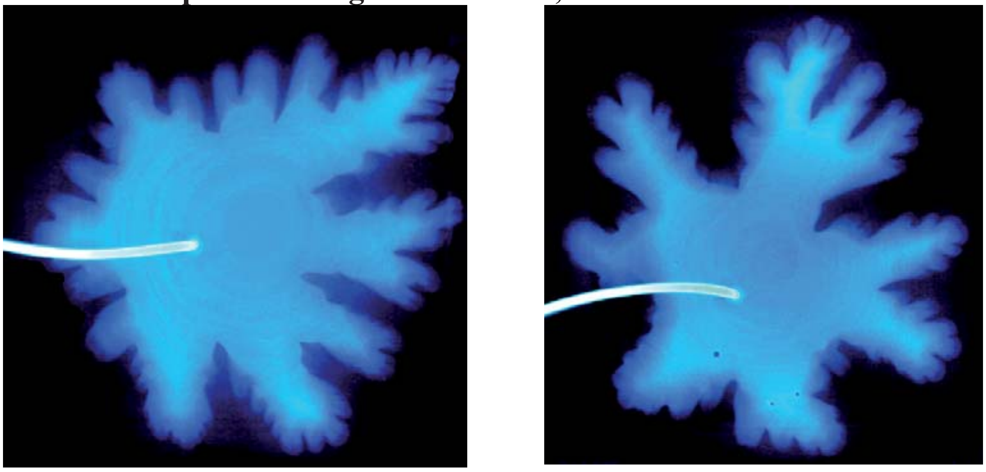
Heptane into light mineral oil; Pressure head: 3 cm

Fig. 23. Injection profiles of miscible Hele-Shaw experiments, in which heptane is injected at a constant head of 3 cm into light mineral oil ($\mu_{\text{LMO}}/\mu_H = 110.7$). Ultrasound at setting 2 (72W) was applied to the cells. The ultrasonically stimulated pattern is compared to the no-ultrasound case (NUS).

(a) Heptane into heavy mineral oil; Pressure head: 5 cm

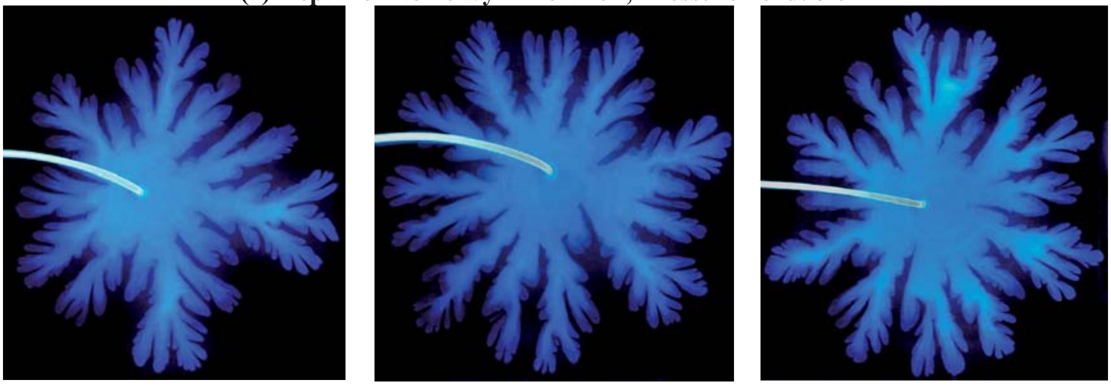

NUS **72 W** **168 W**

(b) Heptane into light mineral oil; Pressure head: 5 cm

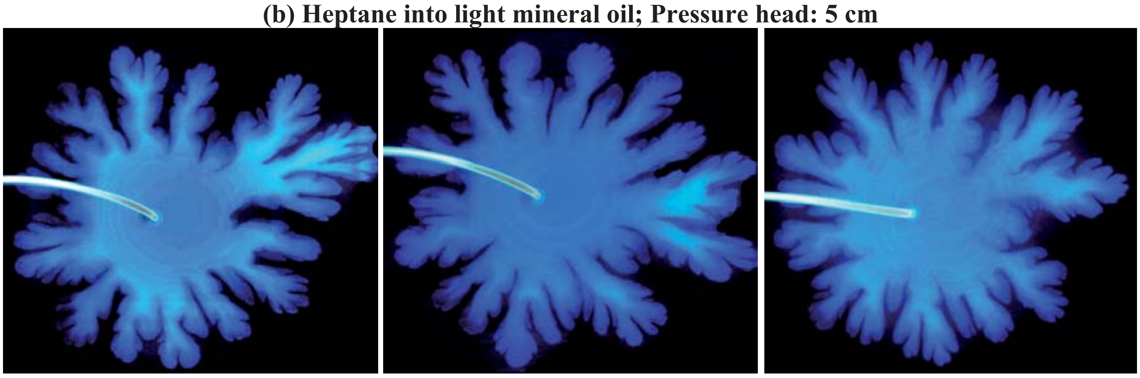

NUS **72 W** **168 W**

Fig. 24. Injection profiles of miscible Hele-Shaw experiments, in which heptane is injected at a constant head of 5 cm into (a) heavy mineral oil ($\mu_{\mathrm{HMO}}/\mu_H = 397.6$) and (b) light mineral oil ($\mu_{\mathrm{LMO}}/\mu_H = 110.7$). Two intensities of ultrasound (setting $2 = 72$ W, setting $5 = 168$ W) were applied to the cells. Patterns are compared to the no-ultrasound case (NUS).

Reducing the interfacial tension of the water seemed to suppress the contribution of ultrasound with heavy mineral oil. On the other hand, light mineral oil responded to a reduction in interfacial tension in a similar manner as with high interfacial tension. Plot of fractal dimension versus modified capillary number leads to the conclusion that ultrasound only perturbs the interfaces of low viscosity oil, and that it is strongly dependent on interfacial tension. Ultrasound is ineffective at higher viscosities, as well as higher injection rate.

We then proceeded with studying the effect of ultrasound on constant pressure displacement. We found that for a broad range of viscosities, ultrasound increases the fractal dimension of the interface. As the viscosity is raised above 1000 cp, however, no discernible change in fractal dimension was observed under ultrasound. A plot of fractal dimension versus viscosity ratio showed that the fractal dimension of the pattern increases with time, and decreases with viscosity ratio. The difference between patters with and without ultrasound is greater at low viscosity ratios, and converges at high viscosity ratios. The rate of increase in fractal dimension as we raise the ultrasonic intensity decreases with increasing viscosity ratio, and increases with increasing pressure. A reduction in interfacial tension did not affect the response of heavy oil to ultrasound. On the other hand, the fractal dimension under ultrasound decreased considerably with a reduction of interfacial tension when light mineral oil was used.

Miscible Hele-Shaw experiments with kerosene and heptane showed that ultrasound improves miscibility of solvents into mineral oil. This is especially true for low injection rates and low pressures, when diffusive mechanisms to dominate. At higher injection rates and pressures, the process is dominated by dispersive viscous displacement, and the mixing zone is not noticeably altered with ultrasound. Ultrasound may be a useful tool to enhance miscible floods and solvent based EOR techniques. More research is necessary in this area.

Lower frequency -seismic- waves found application areas in enhanced oil recovery. High frequency ultrasonic energy could be limited to stimulation of oil-gas wells as they do not show as high travel rate in porous medium as the low frequency waves. Therefore, it may also have a potential use in soil remediation applications. Theoretical studies showed that low frequency waves starts producing much higher frequency waves close to ultrasonic range as they progress in porous medium. This might also be an explanation for remarkable increase in oil recovery observed during seismic activities. In any event, ultrasonic energy has considerable effects on enhanced oil recovery as discussed through this paper and in this regard, understanding the interaction between displacing and displaced fluids is a critical task. We used Hele-Shaw experiments to visually and qualitatively identify the interaction process. We also employed fractal analysis techniques for quantitative identification. The results shed a light on under what circumstances, i.e., flow conditions, oil type, displacing phase properties etc., ultrasonic energy critically effect the interaction process that in turn cause enhancement in oil recovery or removal.

This work was partly funded by an NSERC Grant (No: G121210595). The funds for the equipment used in the experiments were obtained from the Canadian Foundation for Innovation (CFI) (Project # 7566) and the University of Alberta. We gratefully acknowledge these supports. We are also thankful to Dow Chemical Canada Inc. for providing the surfactants samples.

References

1. T. Spanos et al., Journal of Canadian Petroleum Technology, **42**, 16 (2003)
2. R.D. Duhon, J.M. Campbell, *SPE 1316 - The Effect of Ultrasonic Energy on Flow Through Porous Media*, in 2nd Annual Eastern Regional Meeting of SPE/AIME (Charleston, WV, 1965)
3. A.C.T. Aarts et al., SPE Journal **4**, 321 (1999)
4. V.N. Nikolaevskiy et al., SPE Production & Facilities **11**, 89 (1996)
5. O.L. Kuznetsov et al., Journal of Petroleum Science and Engineering **19**, 191 (1998)
6. O.L. Kuznetsov et al., Energy Sources **24**, 877 (2002)
7. T. Hamida, *Effect of Ultrasonic Waves on Immiscible and Miscible Displacement in Porous Media*, University of Alberta, 2006, M.Sc. thesis
8. T. Hamida, T. Babadagli, Transport in Porous Media **70** 2, 231 (2007)
9. T. Hamida, T. Babadagli, *Investigations on the capillary interaction of different oleic and aqueous phases between matrix and fracture under ultrasonic waves*, SPE 94105, SPE EUROPEC / EAGE Annual Conf., 13–16 Jun (2005), Madrid, Spain
10. T. Hamida, T. Babadagli, SPE 92124, SPE Asia Pacific Oil & Gas Conf. and Exh., 5–7 April (2005), Jakarta, Indonesia
11. T. Hamida, T. Babadagli, SPE 95327, 2005 SPE Annual Technical Conference and Exh., Dallas, TX, 9–12 Oct. (2005)
12. T. Hamida, T. Babadagli, *Effects of ultrasonic waves on the interfacial forces between oil and water*, Ultrasonics Sonochemistry, in press, 2007
13. T. Hamida, T. Babadagli, *Effects of ultrasonic waves on the interfacial forces between oil and water*, submitted to *Ultrasonic Sonochemistry* (in review) (2007)
14. P.G. Saffman, G. Taylor, *The Penetration of a Fluid into a Porous Medium or Hele-Shaw Cell Containing a More Viscous Liquid,* Proc. of the Royal Soc. of London Series a-Mathematical and Physical Sciences **245**, 312 (1958)
15. J.W. Mclean, P.G. Saffman, J. Fluid Mechanics **102**, 455 (1981)
16. C.W. Park, G.M. Homsy, Phys. Fluids **28**, 1583 (1985)
17. T. Maxworthy, Journal of Fluid Mechanics **177**, 207 (1987)
18. J.D. Chen, J. Fluid Mechanics **201**, 223 (1989)
19. S.N. Rauseo, P.D. Barnes, J.V. Maher, Phys. Rev. A **35**, 1245 (1987)
20. R.L. Chuoke, P. Vanmeurs, C. Vanderpoel, Transactions of the American Institute of Mining and Metallurgical Engineers **216**, 188 (1959)
21. O. Praud, H.L. Swinney, Phys. Rev. E **72** (2005)
22. X. Guan, R. Pitchumani, Journal of Fluids Engineering-Transactions of the ASME **125**, 354 (2003)
23. G.M. Homsy, Annual Review of Fluid Mechanics **19**, 271 (1987)
24. L. Paterson, Phys. Rev. Lett. **52**, 1621 (1984)
25. T.A. Witten, L.M. Sander, Phys. Rev. Lett. **47**, 1400 (1981)
26. B. Shraiman, D. Bensimon, Phys. Rev. A **30**, 2840 (1984)
27. S.E. May, J.V. Maher, Phys. Rev. A **40**, 1723 (1989)
28. J. Fernandez, G.M. Homsy, Journal of Fluid Mechanics **480**, 267 (2003)
29. G. Daccord, J. Nittmann, Phys. Rev. Lett. **56**, 336 (1986)
30. B.B. Mandelbrot, *The fractal geometry of nature*, updated and augmented (W.H. Freeman, San Francisco, 1983), 468 pp., p. of plates
31. L.S. Liebovitch, T. Toth, Phys. Lett. A **141**, 386 (1989)
32. R.E. Plotnick et al., Phys. Rev. E **53**, 5461 (1996)
33. A. Karperien, *FracLac* V.2 (Charles Stuart University: NSW, Australia, 2005)
34. W.S. Rasband, *ImageJ* (U.S. National Institute of Health: Maryland, USA, 1997-2005)